Plasmon-Enhanced Second Harmonic Sensing

Lavinia Ghirardini, Anne-Laure Baudrion, Marco Monticelli, Daniela Petti, Paolo Biagioni, Lamberto Duò, Giovanni Pellegrini, Pierre-Michel Adam, Marco Finazzi, Michele Celebrano

Plasmon-Enhanced Second Harmonic Sensing

Journal:	*The Journal of Physical Chemistry*
Manuscript ID	jp-2018-03148r.R1
Manuscript Type:	Article
Date Submitted by the Author:	n/a

Complete List of Authors:	Ghirardini, Lavinia; Politecnico di Milano Baudrion, Anne-Laure; ICD-LNIO, Universite de Technologie de Troyes Monticelli, Marco; Politecnico di Milano, Dipartimento di Fisica Petti, Daniela; Politecnico di Milano, Dipartimento di Fisica Biagioni, Paolo; Politecnico di Milano, Physics Duò, Lamberto; Politecnico di Milano, Pellegrini, Giovanni; Politecnico di Milano, Dipartimento Di Fisica Adam, Pierre-Michel; Universite de Technologie de Troyes Finazzi, Marco; Politecnico di Milano, Physics Celebrano, Michele; Politecnico di Milano,

Plasmon-enhanced Second Harmonic Sensing

Lavinia Ghirardini[1], Anne-Laure Baudrion[2], Marco Monticelli[1], Daniela Petti[1], Paolo Biagioni[1], Lamberto Duò[1], Giovanni Pellegrini[1], Pierre-Michel Adam[2], Marco Finazzi[1], Michele Celebrano[1*]

[1] *Dipartimento di Fisica, Politecnico di Milano, piazza Leonardo da Vinci 32, 20133 Milano, Italy*

[2] *Laboratoire de Nanotechnologie et d'Instrumentation Optique, Institut Charles Delaunay, Universite' de Technologie de Troyes, UMR CNRS 6281, 12 Rue Marie-Curie, CS 42060, 10004 Troyes Cedex, France*

[*] *Corresponding author: michele.celebrano@polimi.it*

ABSTRACT

It has been recently suggested that the nonlinear optical processes in plasmonic nanoantennas allow for a substantial boost in the sensitivity of plasmonic sensing platforms. Here we present a sensing device based on an array of non-centrosymmetric plasmonic nanoantennas featuring enhanced second harmonic generation (SHG) integrated in a microfluidic chip. We evaluate its sensitivity both in the linear and nonlinear regime using a figure of merit (FOM $= \frac{\Delta I/I}{\Delta n}$) that accounts for the relative change in the measured intensity, *I*, against the variation of the environmental refractive index *n*. While the signal-to-noise ratio achieved in both regimes allows attaining a resolution (i.e. minimum detectable refractive index variation) $\Delta n_{min} \sim 10^{-3}$, the platform operation in the nonlinear regime features a sensitivity (i.e. the FOM) that is at least 3 times higher than the linear one. Thanks to the surface sensitivity of plasmon-enhanced SHG, our results show that the development of such SHG sensing platforms with sensitivity performances exceeding those of their linear counterparts is within reach.

INTRODUCTION

Optical sensing techniques represent one of the most promising approaches to detect and identify chemical and biological species, thanks to their non-invasive character. In this framework, platforms based on metallic structures featuring collective oscillations of the conduction electrons (surface plasmon resonances, SPRs) have rapidly become a fundamental tool for the real-time, label-free analysis of biospecific interactions and chemical reactions [1]. These sensors allow detecting small amounts of analyte through the variation in reflectivity associated with the SPR shifts induced by the change in the local refractive index caused by the analyte itself [2, 3, 4, 5, 6].

Refractometric plasmonic biosensors have been commercially available for more than 20 years as planar platforms based on propagating surface plasmon polaritons (SPPs) [7]. More recently, platforms based on localized SPR (LSPR) in metallic nanostructures have also been developed. These devices have the potential to overcome the SPP-based approaches, since they exhibit similar molecular sensitivity [8] but require less sophisticated and bulky optical equipment [9]. Moreover, the high-intensity electromagnetic fields associated with the excitation of LSPRs enable a dramatic reduction of the probing volume allowing for single-molecule detection with high temporal resolution [10, 11]. The high-end miniaturization, multiplexing and microfluidics integration, along with the above-listed features, make LSPR substrates promising candidates for high-throughput screening, point-of-care real-time diagnostics, and field applications [6, 12].

The ability of generating and tuning the nonlinear optical processes at the nanoscale remains an open challenge, since it enables the realization of nonlinear optical sensing probes and photonic sources for the next-generation technology. Yet, to date, confinement of nonlinear optical processes beyond the diffraction limit remains a demanding task since phase-matching conditions, which ensure efficient energy transfer from the fundamental to the nonlinear wave in bulk crystals, cannot be exploited in extremely small volumes. To this purpose, the intense local fields associated to SPRs are

an appealing tool to enhance the photon emission rates of nonlinear optical processes. In the last years, significant efforts have been devoted to the understanding of nonlinear optical processes in plasmonic nanostructures, giving rise to the research field of nonlinear plasmonics [13]. The first realization of SHG enhancement via SPRs dates back to the '70s [14]. Since then, the mechanism of nonlinear emission enhancement in metallic nanoparticles has been thoroughly investigated by analyzing the SHG yield as a function of the SPR spectral features. It was soon established that peak SHG is achieved when the plasmonic resonances of the nanoparticles properly matches the wavelengths and polarizations of either the pump beam [15, 16] or that of the SH emission [17]. This led to the development of doubly resonant antennas, to simultaneously enhance the absorption at the pump wavelength and the emission at the SHG wavelength [18] and, hence, boost the local fields at both wavelengths. However, strong local fields alone proved to be insufficient for efficient SHG in centrosymmetric samples like plasmonic materials. For instance, nanostructures possessing axial symmetry showed a silencing effect of the overall SHG intensity in the far-field [19]. It is now recognized that efficient SHG can only be obtained in broken-symmetry configurations, which allow coupling the nonlinear local dipoles to the electric dipole modes of the nanoantennas [15]. To this aim, key strategies based on especially engineered multi-resonant plasmonic antennas have been recently proposed [18, 20, 21, 22, 23, 24]. These approaches combine the ability to enhance and engineer the local fields at both the excitation and the emission wavelength with a tailored emission directionality to improve the nonlinear collection efficiency.

So far, the refractometric plasmonic sensing scheme has been translated to the nonlinear paradigm by only using the third harmonic generation (THG) process [25], demonstrating sensing performances similar to those of linear platforms in terms of signal-to-noise ratio. THG, which stems from the nonlinear currents in the volume of metals, is indeed attained with relatively high yield in plasmonic nanoantennas. Conversely, SHG generally has a very low emission yield in plasmonic nanostructures, since it is inhibited in the volume of metals by parity conservation. Consequently,

SHG arises mainly from the uneven currents at the metal/environment interface and can be enhanced by local imperfections and asymmetries in the local geometry of the antenna or in the environment. Therefore, despite the low emission yield, its surface character makes plasmon-enhanced SHG a very promising tool for plasmonic sensing and, recently, inspired the development of various concepts based on plasmon-enhanced SHG sensing [22, 26]. In this framework, remarkable performances both in terms of FOMs and minimum detectable refractive index have been theoretically reported exploiting quadrupolar [27] and Fano-like [28] resonances in plasmonic nanoparticles.

In this work, we realize and characterize a first platform prototype for plasmon-enhanced SHG sensing based on dense ordered arrays of L-shaped Au nanoantennas fabricated on glass and encapsulated in a microfluidic device. We compare its linear and nonlinear sensing performances by monitoring the variation of the sample reflectance at the pump fundamental wavelength (FW) and of the SHG yield, upon changing the refractive index of the environment. This is achieved by putting our sample in contact with three solutions of water and ethanol at different concentrations. These periodic arrays demonstrated an enhanced SHG thanks to the lack of inversion symmetry of each single element, a double resonance at both the FW and the second harmonic (SH) wavelength, along with a sizeable spatial overlap between the plasmonic modes associated with such resonances. In addition, they feature a high directionality in the emission pattern of the SHG that allows for efficient signal collection in a relatively narrow solid angle, hence enabling the use of low NA optical detection systems [29, 30, 31, 32, 33, 34] although at the expenses of the overall SHG efficiency [29].

EXPERIMENTAL SECTION

The investigated sample comprises two identical sets of six arrays of L-shaped gold antennas (see Figure 1a), called pads from now on for the sake of simplicity. The nanoantenna arms within each pad are 50-nm-thick and 40-nm-wide and arranged in a periodic square lattice with a gap of 100 nm between adjacent antennas (see Figure 1b). Each pad is characterized by antennas featuring the same

arm-length L that varies from 135 to 285 nm in steps of 30 ± 2 nm for each pad, to tune the LSPR at different wavelengths. The plasmonic platform design and fabrication by electron-beam lithography are detailed elsewhere [29] along with its nonlinear characterization in air environment.

The device is equipped with a microfluidic channel (100 µm wide and 30 µm high) in polydimethylsiloxane (PDMS), fabricated by soft-lithography and bonded to the glass substrate with an oxygen plasma treatment. One of the two sets of pads is encapsulated inside the microfluidic channel, whereas the PDMS sticks directly onto the second set of pads (see Figure 1a), isolating it from the fluid. The latter set of pads serves as a real-time reference for the sensing experiment, since it is provided with a constant environmental refractive index (n = 1.4) during the entire experiment. The tested solutions are volume mixtures of $(1 - x)$ pure deionized water (H_2O) and x ethanol, with x = 0, 0.25 and 0.5 that flow through the channel thanks to a syringe pump and are collected at the output in a drain below the sample level. Between subsequent acquisitions, the channel is emptied and air is flown to make sure that the previous solution is completely removed and that the channel is dry before flowing the next liquid.

In the linear sensing configuration, a change in the refractive index of the environment, Δn, causes a frequency shift, $\Delta\omega$, in the LSPR of the antennas, which translates into a variation of the detected reflected intensity, ΔI_ω, at the pump frequency, ω. Since the SHG yield depends quadratically on the field intensity enhancement produced by the antenna resonance, a change in Δn is expected to induce a sizeable variation in the SHG intensity, $\Delta I_{2\omega}$. The figures of merit (FOM) that we will analyze are then $\Delta(I/I_{\mathrm{ref}})_\omega/\Delta n$ and $\Delta(I/I_{\mathrm{ref}})_{2\omega}/\Delta n$ for the linear and nonlinear case, respectively [35]. In both expressions, I_{ref} represents the reflected or the SHG intensity recorded on the reference pads placed under the PDMS. The signals coming from the sensing pads (I_ω and $I_{2\omega}$) are normalized by the intensities I_{ref} of each corresponding reference pad to compensate for possible laser fluctuations and slow system drifts. This normalization is applied on the average signals from each pad as evaluated from the spatial maps measured with an integration time of 10 s/line. Both the reflectivity and SHG

signal of the pads are monitored using a standard home-built inverted microscope (see Figure 1c). The femtosecond pulses ($\Delta\tau \sim 150$ fs) from an Er-doped fiber laser are linearly polarized (~10^2:1) to best excite the fundamental mode of the antennas around 1550 nm, and focused on the sample through a 0.7-NA long-working-distance air objective. The signal from the sample is then collected in epi-reflection geometry through the same objective and it is sent to the detection path through a non-polarizing beam-splitter. A dichroic mirror (DMSP1000, Thorlabs Inc.) separates the nonlinear emission from the FW coming from the device, which is reflected onto a commercial InGaAs photodiode (PDA20CS, Thorlabs Inc.) to monitor the linear reflectivity. The nonlinear emissions is further filtered by a narrow bandpass filter (centered around 775 nm with a 25-nm bandwidth) to isolate the SHG peak from photoluminescence and residual FW light and is detected with a silicon single photon avalanche diode (PDM Series-C module, MPD Srl). The linear and nonlinear maps are collected by raster-scanning a piezoelectric stage (P517-3CL, Physik Instrumente GmbH), after the solutions with different refractive indices reach a static condition in the microfluidic channel.

RESULTS

Figure 2 shows the FW (a) and SHG (b) maps collected by exciting the sample with 800 μW average power. The reference pads are the ones on the right, as confirmed by the fact that their intensity does not significantly change through the different measurements. The set of pads exposed to the solutions is the one on the left in each panel. One can immediately recognize that, as expected, the resonance shifts to shorter antennas (i.e. a red-shift in the resonance) as the environment refractive index is progressively increased (this is especially evident if one compares the behavior in Air with that in pure H_2O, where the step index change is about 30%). This trend can be observed both in the linear (Fig. 2a) and nonlinear (Fig. 2b) maps. Due to the well-known change in the radiation pattern of the generated light that favors emission towards the higher refractive index region [36, 37], an intensity variation can be easily observed (especially in the SHG map) when the nanoantennas are measured

in the solution with respect to air. The rise in the environmental refractive index induced by flowing a water-ethanol mixture in the channel increases the emission of light towards the upper half-space – i.e. away from the collection path – thus reducing the measured signal. The SHG intensity from the gold stripe in the middle of the sample (clearly visible in the FW maps), used for alignment purpose, remains below the detection threshold with the applied integration times and pump fluency, hence further evidencing the strong SHG yield of the antenna arrays.

The shift of the resonance is more clearly visible in Fig. 3, by comparing both the FW reflectance and the SHG emission of the signal pads (panels a and c) with those of the reference pads under PDMS (panels b and d) for the different refractive indices. Each point represents the average emission from a pad during four different scans using the same solution, while the full error bar corresponds to twice the standard deviation σ of the average process, hence reflecting the measurement repeatability. Each scan covers the whole sample and lasts approximately 10-20 minutes. The resonance profiles from the reference pads are almost identical for the different solutions, both in the linear (Fig. 3b) and nonlinear (Fig. 3d) measurements. A comparison between the two panels also indicates a slight red shift occurring between the FW resonance and the SHG one (i.e. higher SHG yield is displayed at shorter arm lengths with respect to the peak reflectance), as already reported in literature [16, 38, 39].

Figure 3e shows the emission power curves acquired on each pad. The quadratic behavior of the SHG signal dependence on the pump power confirms that the measured signal comes from a two-photon excitation process, while the measurements repeatability yields no indication of photodamage. It is worth mentioning that, although here we select SHG using a narrow band filter, two-photon photoluminescence from gold in the visible region is dramatically reduced when pumping at telecom wavelengths [20].

Figure 4 shows the evolution of both the normalized reflectivity (panel a) and SHG emission (panel b) from the antennas as the environmental refractive index *n* is changed. Each point represents the

average intensity either reflected or emitted from each individual pad normalized by that of the refence pad under PDMS, $(I/I_{\mathrm{ref}})_{\omega}$ or $(I/I_{\mathrm{ref}})_{2\omega}$. Considering an integration time of about 10 ms per pixel in the maps, in our experimental realization we arrive to about 1 min acquisition time for each experimental data point, which is compatible with that of previously-reported nonlinear sensing experiments [25].

DISCUSSION

By relating Figs. 4 to Fig. 3, one can readily notice that the dependence of the linear reflectivity on the plasmonic resonance of the nanoantennas as *n* changes is the one expected for standard LSPR refractometric sensing. In fact, the variation of the normalized FW reflectivity, which is the slope of the linear fit to the data in Fig. 4, as the arm length of the nanoantennas is increased (see panel a to f) is larger for the device featuring the shortest arm length (pad 1, 140 nm), it decreases when the resonant pad is approached (pad 4, 230 nm) and it changes sign increasing its absolute value for longer arm length (pads 5, 260 nm and 6, 290 nm). In fact, the geometrical parameters are such that when the pad response lies on the inflection points of the resonance at the FW (see Fig. 3c), a shift in the resonance curve – caused by the variation in the refractive index – induces the maximum signal variation. Conversely, close to the resonance peak the intensity variation $(\Delta I/I_{\mathrm{ref}})_{\omega}$ reaches a minimum. In other words, an increase in the refractive index induces a red shift in the resonance (see Fig. 3a and c), therefore the resonant condition is met progressively towards shorter arm lengths, hence determining a boost (drop) of the probe signal when the pump frequency is higher (lower) than the resonance frequency of the antennas.

It is now interesting to address the SHG sensing performances of this platform and compare them to the linear ones. To evaluate the intrinsic sensitivity of each device, we computed the FOM values by the slope of each graph both in the linear and nonlinear regime, $(\Delta I/I_{\mathrm{ref}})_{\omega}/\Delta n$ and $(\Delta I/I_{\mathrm{ref}})_{2\omega}/\Delta n$ (see Fig. 5a). Higher values of the FOM are found for pad 1 (140 nm) and are up to about 30 and 10

in the SHG and FW regime, respectively. Therefore, in this platform, plasmon-enhanced SHG sensing reaches up to 3 times a higher sensitivity with respect to the linear regime with absolute values of the FOM that are comparable to and even higher than those of other highly-efficient linear plasmonic sensing platforms [40, 41].

To attain a comprehensive comparison between the linear and nonlinear performances of the platform, we also determined its detection limits in both regimes by estimating the minimum measurable variation in the refractive index, $\Delta n_{\min}$ (see Fig. 5b) [20]. This quantity, which is commonly referred to as "resolution" in SPR sensing [42], allows to assess the platform sensitivity (FOM) against the signal-to-noise ratio of the measure. We obtain $\Delta n_{\min}$ dividing the average between the error bars in each panel of Fig. 4 (i.e. minimum detectable intensity variation) by the slope of the linear fit in the same panel. Analyzing pad 1 (140 nm) according to this parameter, we find $\Delta n_{\min}^{2\omega} = \frac{(\Delta I/I_{\mathrm{ref}})_{\min}}{(\Delta I/I_{\mathrm{ref}})_{2\omega}/\Delta n} \sim 1.2 \times 10^{-3}$ and $\Delta n_{\min}^{\omega} \sim 6 \times 10^{-4}$ in the nonlinear and linear regime, respectively. By evaluating $\Delta n_{\min}$ for all pads in both regimes, we find that in the linear regime the best-performing devices are pads 5 (260 nm) and 6 (290 nm), featuring $\Delta n_{\min}^{\omega} \sim 4 \times 10^{-4}$, which is 3 times lower than the $\Delta n_{\min}^{2\omega}$ of pad 1 (140 nm, i.e. the best in the nonlinear regime). The same pads, being out of resonance with respect to the FW, show significant performance degradation in the nonlinear regime due to the SHG signal drop. Comparable results were obtained on different samples realized using the same nominal fabrication parameters ($\Delta n^{2\omega}{}_{\min} \sim 0.9 \div 2 \times 10^{-3}$ and $\Delta n^{\omega}{}_{\min} \sim 6 \times 10^{-4}$). Given the discretization applied to the arm lengths, we ascribe these oscillations in the determination of $\Delta n_{\min}$ to uncertainties in the actual antenna geometry for the same fabrication parameters. It is here worth noting that both sensing mechanisms display higher FOM values and resolution for pads with arm length shorter than the resonant geometry (see Fig. 5a), corresponding to the inflection points of the resonance (see Fig. 3a, c). Conversely, the two sensing mechanisms behave differently on resonance. As expected, in the linear regime the FOM values drop to zero and concurrently the resolution ($\Delta n_{\min}$) decreases, while

in the nonlinear regime the FOM value remains sizeable even on resonance (pad 3). This allows achieving a high resolution also on the resonant pad (pad 3), where we have the largest SHG signal, suggesting that the resonant behavior at the FW alone is not sufficient to account for our experimental observation, conversely to what has been reported in other nonlinear refractometric experiments [25]. Indeed, the resonant conditions at the SH wavelength, the coupling between the FW and the SH modes as well as the selection rules for efficient SHG emission might play a significant role in this nonlinear sensing mechanism.

CONCLUSIONS

By analyzing the performances of a plasmonic sensing platform in both the linear and nonlinear regime when the environmental refractive index is varied, we found similar performances in terms of the minimum detectable refractive index Δn_{min}. This result, as already highlighted in a recent paper on THG plasmonic sensing [25], seems to put the linear and nonlinear regimes on an equal footage, with the former slightly favored due to its simpler implementation. Nevertheless, plasmon-enhanced SHG sensing still holds promise to overcome plasmonic sensing schemes working in the linear regime, thanks to the nonlinear dependence on the local field enhancements. In fact, the FOM of these L-shaped nanoantenna-based platforms in the nonlinear regime (i.e. ~ 30) are significantly higher than that featured in the linear regime by the same platform and by other effective platforms [40, 41]. Yet, despite offering a good tradeoff between nanostructure simplicity and their nonlinear efficiency, these devices are not quite fully optimized for efficient SHG [20]. By engineering the nanoantenna geometries to attain higher nonlinearities together with a nonlinear setup with a higher signal-to-noise ratio, combined with a dual-beam real-time referencing, nonlinear plasmonic sensing platforms have the potential to overcome standard linear platforms. This could also be favored by the physical mechanisms at work in plasmon-enhanced SHG platforms, where the local binding of a

nano-object to the hot spot region in properly functionalized platforms strongly modifies the local symmetry of the system and might promote further SHG modulation.

ACKNOWLEDGEMENTS

The authors would like to thank Prof. R. Bertacco for fruitful discussions on the microfluidic part. As the nanofabrication process was carried out through the facilities of the Nano'Mat platform (www.nanomat.eu), the authors acknowledge the financial supports from the "Ministère de l'Enseignement Supérieur et de la Recherche", the "Conseil Régional Champagne-Ardenne", the "Fonds Européen de Développement Régional (FEDER) fund", and the "Conseil Général de l' Aube". This work has been carried out in the framework of Cost Action MP1302 Nanospectroscopy. The authors would also like to acknowledge the financial support of Cariplo Foundation through Project SHAPES (2013-0736).

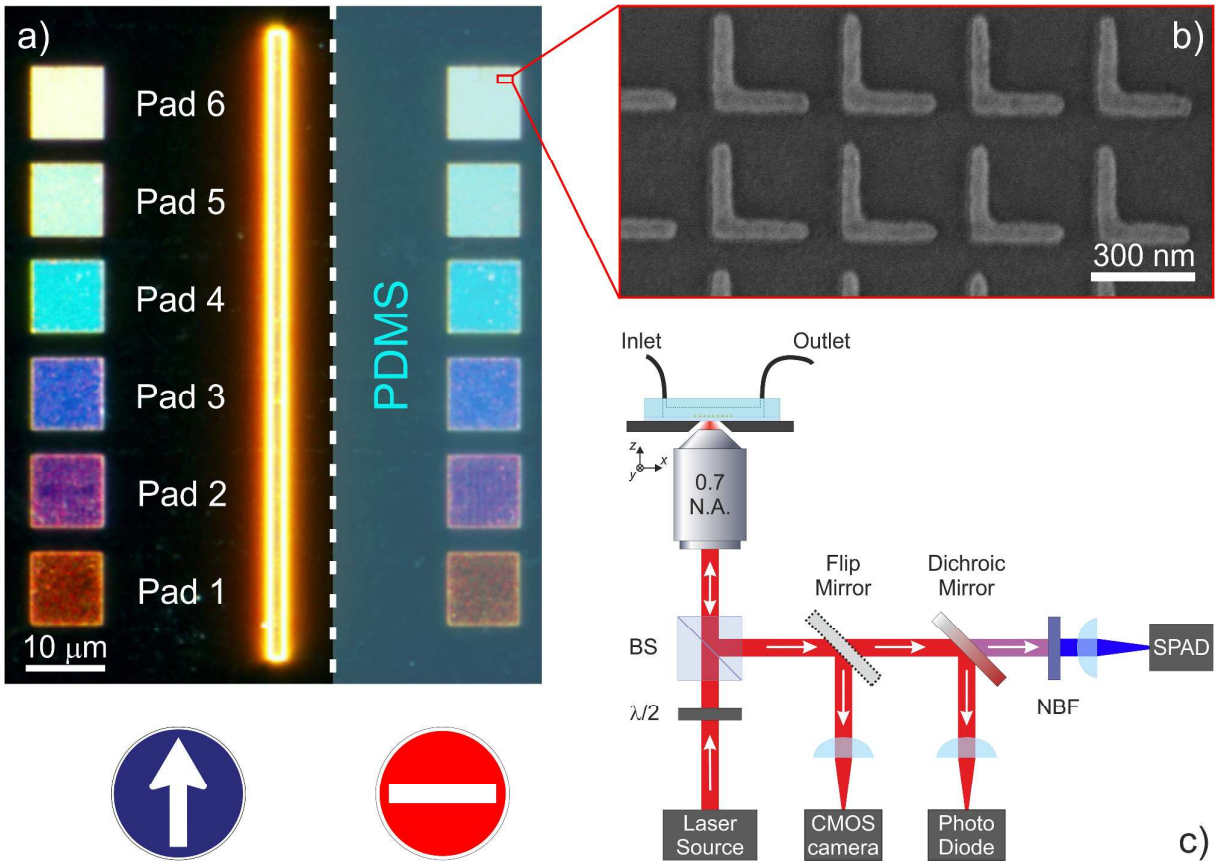

Figure 1: (a) Dark-field reflection map of one of the plasmonic platforms. The L-shaped antennas are arranged in two columns of six 10 µm × 10 µm square lattices on a glass substrate. The right column, covered by PDMS (transparent light-blue layer), is used as a reference to normalize the signal collected from the left column. The gold stripe in the middle is used for the microfluidic channel alignement. The arm length parameter L associated to each pad is pad 1 = 140 nm, pad 2 = 170 nm, pad 3 = 200 nm, pad 4 = 230 nm, pad 5 = 260 nm, pad 6 = 290 nm. (b) Scaning electron microscopy map of the array with arm-length 290 nm (pad 6 – area maked red in panel a), recorded at a very low acceleration voltage on the non-conductive substrate. (c) Experimental setup. Laser source: Er-doped fiber laser (150-fs-long pulses at 80 MHz centered at 1554 nm). BS: non-polarizing beam-splitter. Dichroic mirror: DMSP1000 (Thorlabs Inc.). PhotoDiode: infrared InGaAs photodiode (Thorlabs Inc.). NBF: narrow band pass filter (775 nm / 25 nm badwidth). SPAD: single photon avalanche diode (PDM Series-C module, MPD S.r.l.).

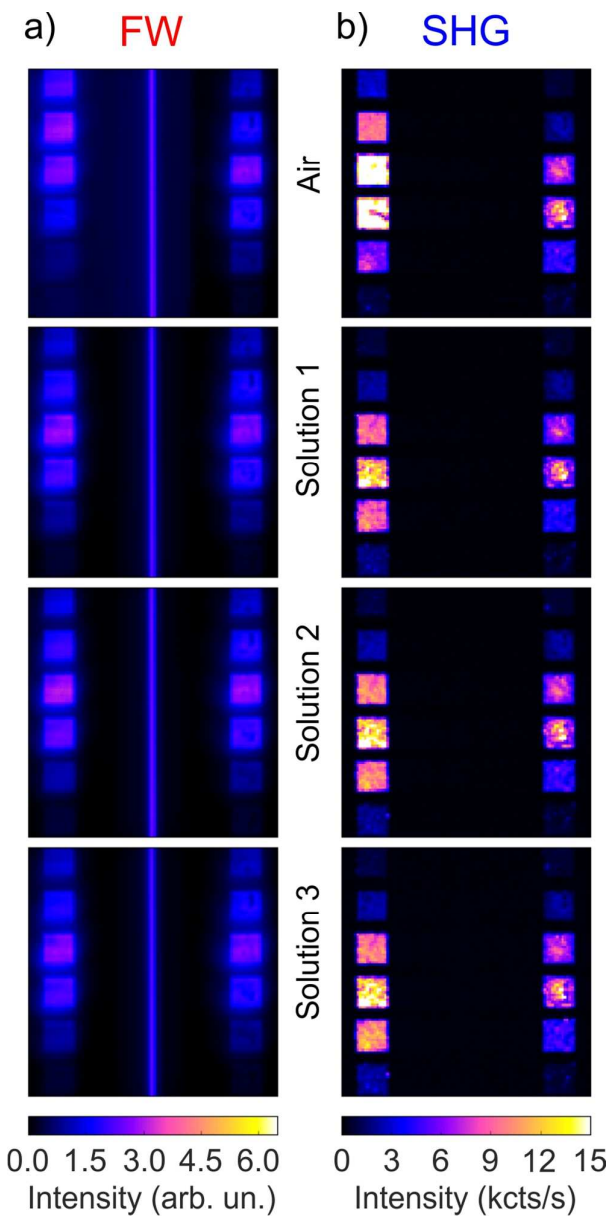

Figure 2: Linear (a) and nonlinear (b) maps recorded with the setup described in Figure 1b. The higher SHG yield is achieved on pad 3 (arm length L = 200 nm), in agreement with what reported in Ref. 21. The array of pads on the right-hand side of each panel lies under the PDMS and thus remains in a constant refractive index throughout the entire experiment. The pads on the left-hand side are located inside the microfluidic channel (see the brigther background in the top-left panel) and the environmental refractive index they experience is changed during the different measurements. The tested solutions are volume mixtures of $(1-x)$ pure deionized water and x ethanol (Solution 1: $x = 0$, Solution 2: $x = 0.25$, Solution 3: $x = 0.5$).

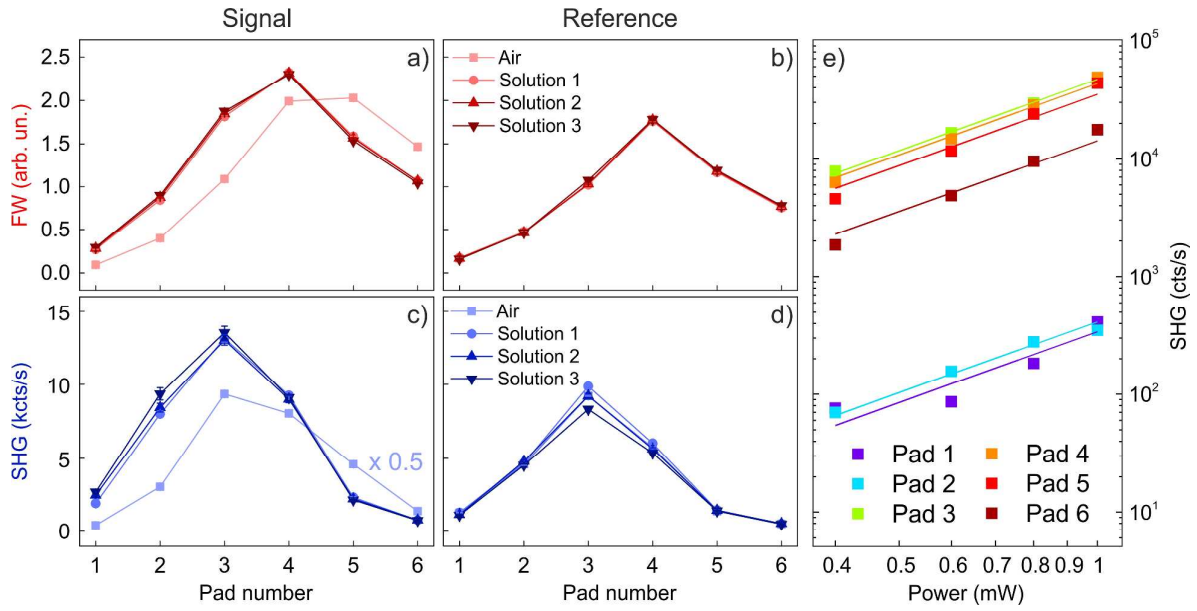

Figure 3: Evolution of the pads emission at the SHG wavelength (a, b) and of their reflectance at the fundamental wavelength (c, d) from both the signal and the reference pads. The tested solutions are volume mixtures of $(1 - x)$ pure deionized water and x ethanol (Solution 1: $x = 0$, Solution 2: $x = 0.25$, Solution 3: $x = 0.5$). (e) Power curves for the pads in air. Straight lines are quadratic fits to the data. The arm length parameter L associated to each pad is pad 1 = 140 nm, pad 2 = 170 nm, pad 3 = 200 nm, pad 4 = 230 nm, pad 5 = 260 nm, pad 6 = 290 nm.

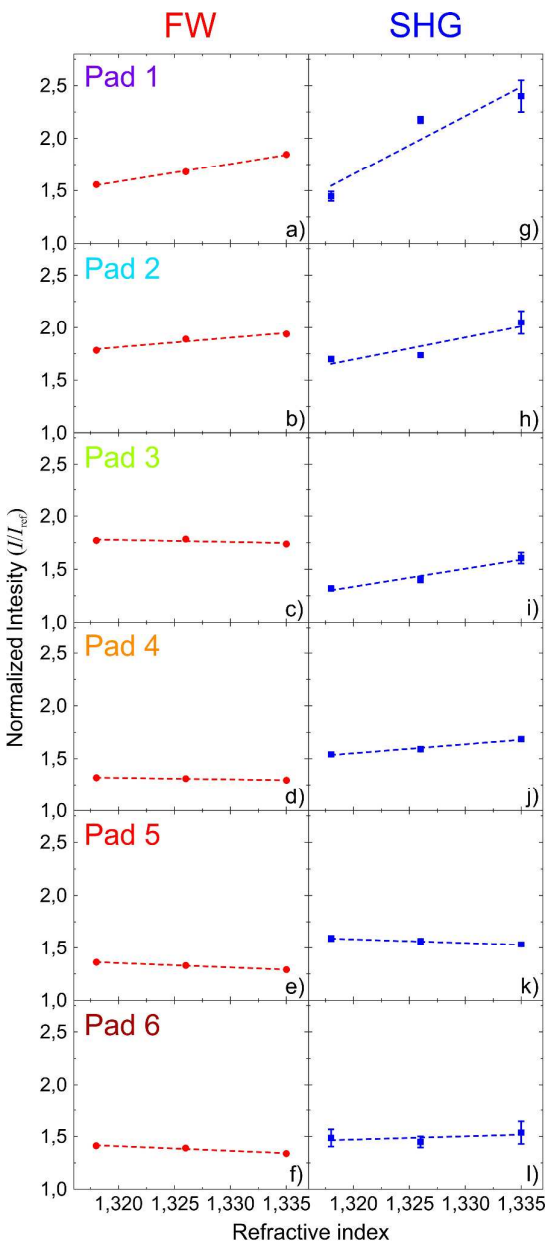

Figure 4: Evolution of the normalized FW reflectivity (left column, red dots) and of the normalized SHG (right column, blue squares) recorded from the six pads as a function of the environmental refractive index for the three different solutions. The error bars are obtained from the average process between four subsequent measurements and in panels a-f (i.e. the measurements at the FW) are confined within the dot.

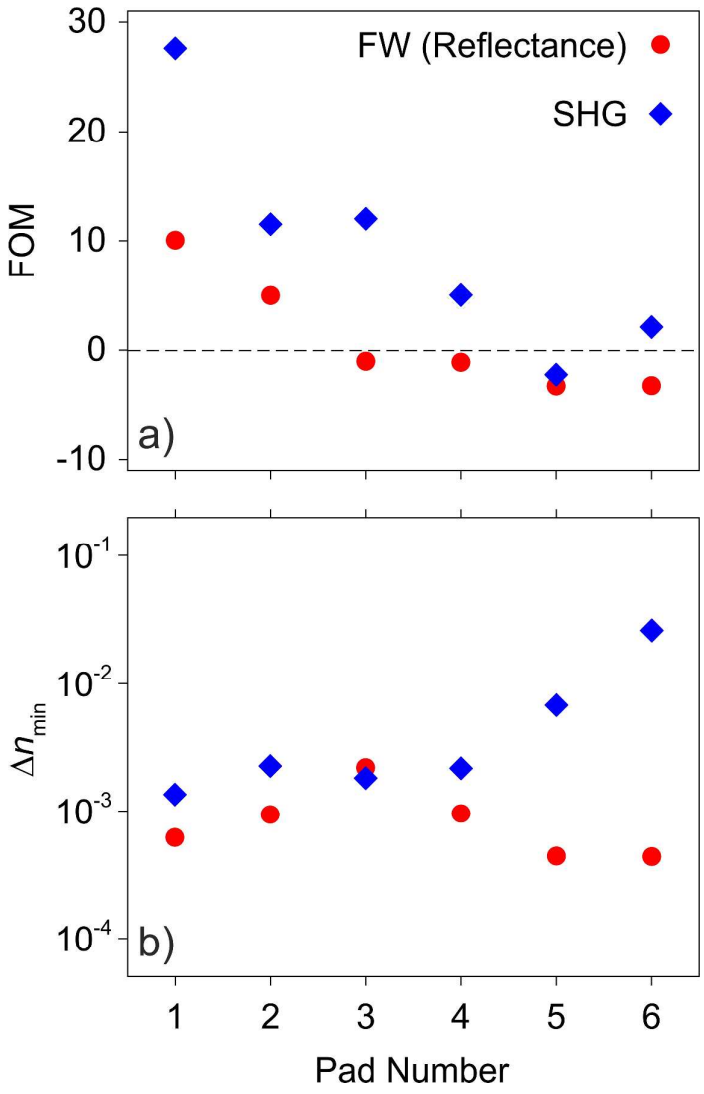

Figure 5: a) FOM (i.e. sensitivity) of each pad that composes our sensing platform, evaluated in both the linear (red dots) and nonlinear (blue diamonds) regime, respectively. The error bars, which represent the error associated with the linear fit of each panel in Figure 4, are confined within the dots. b) Minimum detectable refractive index variation, Δn_{min}, by each pad in our sensing platform plotted in Log scale and obtained in both the linear (red dots) and nonlinear (blue diamonds) regime, respectively.

REFERENCES

[1] Maier, S. A. Plasmonics: Fundamentals and Applications. *Springer* **2007**.

[2] Li, M.; Cushing, S. K.; Wu, N. Plasmon-enhanced Optical Sensors: A Review. *Analyst* **2015**, *140*, 386-406.

[3] Zhao, Y.; Cao, L.; Ouyang, J.; Wang, M.; Wang, K.; Xia, X.-H. Reversible Plasmonic Probe Sensitive for pH in Micro/Nanospaces Based on i-Motif-Modulated Morpholino-Gold Nanoparticle Assembly. *Anal. Chem.* **2013**, *85*, 1053–1057.

[4] Virk, M.; Xiong, K.; Svedendahl, M.; Käll, M.; Dahlin, A. B. A Thermal Plasmonic Sensor Platform: Resistive Heating of Nanohole Arrays. *Nano Lett.* **2014**, *14*, 3544–3549.

[5] Langhammer, C.; Zorić, I.; Kasemo, B. Hydrogen Storage in Pd Nanodisks Characterized with a Novel Nanoplasmonic Sensing Scheme. *Nano Lett.* **2007**, *7*, 3122–3127.

[6] Acimovic, S.; Ortega, M. A.; Sanz, V.; Berthelot, J.; Garcia-Cordero, J. L.; Renger, J.; Maerkl, S. J.; Kreuzer, M. P.; Quidant, R. LSPR Chip for Parallel, Rapid, and Sensitive Detection of Cancer Markers in Serum. *Nano Lett.* **2014**, *14*, 2636–2641.

[7] Editorial. Commercializing Plasmonics. *Nat. Photonics* **2015**, *9*, 477.

[8] Svedendahl. M.; Chen, S.; Dmitriev, A.; Käll, M. Refractometric Sensing Using Propagating Versus Localized Surface Plasmons: A Direct Comparison. *Nano Lett.* **2009**, *9*, 4428–4433.

[9] Mayer, K. M.; Hafner, J. H. Localized Surface Plasmon Resonance Sensors. *Chem. Rev.* **2011**, *111*, 3828–3857.

[10] Rosman, C.; Prasad, J.; Neiser, A.; Henkel, A.; Edgar, J.; Sönnichsen, C. Multiplexed Plasmon Sensor for Rapid Label-Free Analyte Detection. *Nano Lett.* **2013**, *13*, 3243–3247.

[11] Ament I.; Prasad, J.; Henkel, A.; Schmachtel, S.; Sönnichsen, C. Single Unlabeled Protein Detection on Individual Plasmonic Nanoparticles. *Nano Lett.* **2012**, *12*, 1092–1095.

[12] Anker, J. N.; Hall, W. P.; Lyandres, O.; Shah, N. C.; Zha, J.; Van Duyne, R. P. Biosensing with Plasmonic Nanosensors. *Nat. Mater.* **2008**, *7*, 442–453.

[13] Kauranen, M.; Zayats, A. V. Nonlinear Plasmonics. *Nat. Photonics* **2012**, *6*, 737–748.

[14] Simon, H.; Mitchell, D.; Watson, J. Optical Secondary-harmonic Generation with Surface Plasmons in Silver Films. *Phys. Rev. Lett*. **1974**, *12*, 1531–1534.

[15] Sandrock, M. L.; Pibel C. D.; Geiger, F. M; Foss, C. A. Synthesis and Second-Harmonic Generation Studies of Noncentrosymmetric Gold Nanostructures. *J. Phys. Chem. B* **1999,** *103*, 2668-2673.

[16] Hubert, C.; Billot, L.; Adam, P.-M.; Bachelot, R.; Royer, P.; Grand, J.; Ginder, D.; Dorkenoo, K. D.; Fort, A. Role of Surface Plasmon in Second Harmonic Generation from Gold Nanorods. *Appl. Phys. Lett.* **2007**, *90*, 181105.

[17] Antoine, R.; Galletto, P.; Brevet, P. F.; Pellarin, M.; Prével, B.; Palpant, B.; Girault, H. H.; Broyer, M. Surface Plasmon Enhanced Second Harmonic Response from Gold Clusters Embedded in an Alumina Matrix. *J. Appl. Phys* **1998**, *84*, 4532-1998.

[18] Thyagarajan, K.; Rivier, S.; Lovera, A.; Martin, O. J. F. Enhanced Second-Harmonic Generation from Double Resonant Plasmonic Antennae. *Opt. Express* **2012**, *20*, 12860–12865.

[19] Berthelot, J.; Bachelier, G.; Song, M.; Rai, P.; des Francs, G. C.; Dereux, A.; Bouhelier, A. Silencing and Enhancement of Second-harmonic Generation in Optical Gap Antennas. *Opt. Express* **2012**, *20*, 10498–10508.

[20] Celebrano M.; Wu, X.; Baselli, M.; Großmann, S.; Biagioni, P.; Locatelli, A.; De Angelis, C.; Cerullo, G.; Osellame, R.; Hecht, B.; et al. Mode Matching in Multiresonant Plasmonic Nanoantennas for Enhanced Second Harmonic Generation. *Nat. Nanotechnol.* **2015**, *10*, 412–417.

[21] Metzger, B.; Hentschel, M.; Schumacher, T.; Lippitz, M.; Ye, X.; Murray, C. B.; Knabe, B.; Buse, K.; Giessen, H. Doubling the Efficiency of Third Harmonic Generation by Positioning ITO Nanocrystals into the Hot-spot of Plasmonic Gap-antennas. *Nano Lett.* **2014**, *14*, 2867–2872.

[22] Butèt J.; Brevet, P.-F.; Martin, O. J. F. Optical Second Harmonic Generation in Plasmonic Nanostructures: From Fundamental Principles to Advanced Applications. *ACS Nano* **2015**, *9*, 10545–10562.

[23] Aouani, H.; Rahmani, M.; Navarro-Cía, M.; Maier, S. A. Third-harmonic Upconversion Enhancement from a Single Semiconductor Nanoparticle Coupled to a Plasmonic Antenna. *Nat. Nanotechnol.* **2014**, *9*, 290–294.

[24] Aouani, H.; Navarro-Cia, M.; Rahmani, M.; Sidiropoulos, T. P. H.; Hong, M.; Oulton, R. F.; Maier, S. A. Multiresonant Broadband Optical Antennas as Efficient Tunable Nanosources of Second Harmonic Light. *Nano Lett.* **2012**, *12*, 4997–5002.

[25] Mesch, M.; Metzger, B.; Hentschel, M.; Giessen, H. Nonlinear Plasmonic Sensing. *Nano Lett.* **2016**, *16*, 3155–3159.

[26] Ray, P. C. Size and Shape Dependent Second Order Nonlinear Optical Properties of Nanomaterials and Their Application in Biological and Chemical Sensing. *Chem. Rev.* **2010**, *110*, 5332–5365.

[27] Butet, J.; Russier-Antoine, I.; Jonin, C.; Lascoux, N.; Benichou, E.; Brevet, P.-F. Sensing with Multipolar Second Harmonic Generation from Spherical Metallic Nanoparticles. *Nano Lett.* **2012**, *12*, 1697–1701.

[28] Butet J.; Martin O. J. F. Refractive Index Sensing with Fano Resonant Plasmonic Nanostructures: A Symmetry Based Nonlinear Approach. *Nanoscale* **2014**, *6*, 15262–15270.

[29] Baselli, M.; Baudrion, A.-L.; Ghirardini, L.; Pellegrini, G.; Sakat, E.; Carletti, L.; Locatelli, A.; De Angelis, C.; Biagioni, P.; Duò, L.; at al. Plasmon-Enhanced Second Harmonic Generation: From Individual Antennas to Extended Arrays. *Plasmonics* **2016**, *12*, 1595–1600.

[30] Black L.-J.; Wiecha, P. R.; Wang, Y.; de Groot, C. H.; Paillard, V.; Girard, C.; Muskens, O. L.; Arbouet, A. Tailoring Second-harmonic Generation in Single L-shaped Plasmonic Nanoantennas from the Capacitive to Conductive Coupling Regime. *ACS Photonics* **2015**, *2*, 1592–1601.

[31] Keren-Zur, S.; Avayu, O.; Michaeli, L.; Ellenbogen, T. Nonlinear Beam Shaping with Plasmonic Metasurfaces. *ACS Photonics* **2016**, *3*, 117–123.

[32] Czaplicki, R.; Kiviniemi, A.; Laukkanen, J.; Lehtolahti, J.; Kuittinen, M.; Kauranen, M. Surface Lattice Resonances in Second-harmonic Generation from Metasurfaces. *Opt. Lett.* **2016**, *41*, 2684-2687.

[33] Stokes N.; Cortie, M. B.; Davis, T. J.; McDonagh, A. M. Plasmon Resonances in V-shaped Gold Nanostructures. *Plasmonics* **2012**, *7*, 235–243.

[34] Vercruysse, D.; Sonnefraud, Y.; Verellen, N.; Fuchs, F. B.; Di Martino, G.; Lagae, L.; Moshchalkov, V. V.; Maier, S. A.; Van Dorpe, P. Unidirectional Side Scattering of Light by a Single-element Nanoantenna. *Nano Lett.* **2013**, *13*, 3843–3849.

[35] Becker, J.; Trügler, A.; Arpad Jakab, A.; Hohenester, U.; Sönnichsen, C. The Optimal Aspect Ratio of Gold Nanorods for Plasmonic Bio-sensing. *Plasmonics* **2010**, *5*, 161–167.

[36] Lukosz W.; Kunz, R. E. Light Emission by Magnetic and Electric Dipoles Close to a Plane Interface. I. Total Radiated Power. *J. Opt. Soc. Am.* **1977**, *67*, 1607-1615.

[37] Chung. K.; Tomljenovic-Hanic, S. Emission Properties of Fluorescent Nanoparticles Determined by Their Optical Environment. *Nanomaterials* **2015**, *5*, 895–905.

[38] Metzger, B.; Gui, L.; Fuchs, J.; Floess, D.; Hentschel, M.; Giessen, H. Strong Enhancement of Second Harmonic Emission by Plasmonic Resonances at the Second Harmonic Wavelength. *Nano Lett.* **2015**, *15*, 3917–3922.

[39] Celebrano, M.; Savoini, M.; Biagioni, P.; Zavelani-Rossi, M.; Adam, P.-M.; Duò, L.; Cerullo, G.; Finazzi, M. Retrieving the Complex Polarizability of Single Plasmonic Nanoresonators, *Phys. Rev. B* **2009**, *80*, 153407.

[40] Cattoni, A.; Ghenuche, P.; Haghiri-Gosnet, A.-M.; Decanini, D.; Chen, J.; Pelouard, J.-L.; Collin, S. λ^3/1000 Plasmonic Nanocavities for Biosensing Fabricated by Soft UV Nanoimprint Lithography. *Nano Lett.* **2011**, I, 3557–3563.

[41] Lodewijks, K.; Van Roy, W.; Borghs, G.; Lagae, L.; Van Dorpe, P. Boosting the Figure-Of-Merit of LSPR-Based Refractive Index Sensing by Phase-Sensitive Measurements. *Nano Lett.* **2012**, *12*, 1655–1659.

[42] Homola, J. Surface Plasmon Resonance Sensors for Detection of Chemical and Biological Species. *Chem. Rev.* **2008**, *108*, 462–493.

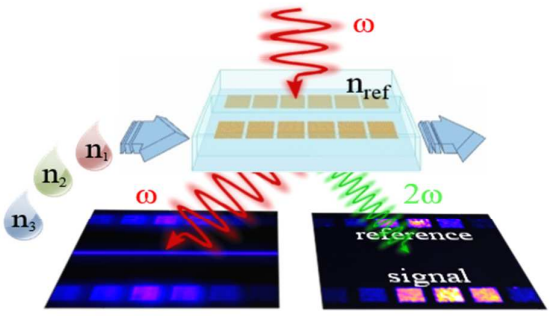

TOC figure

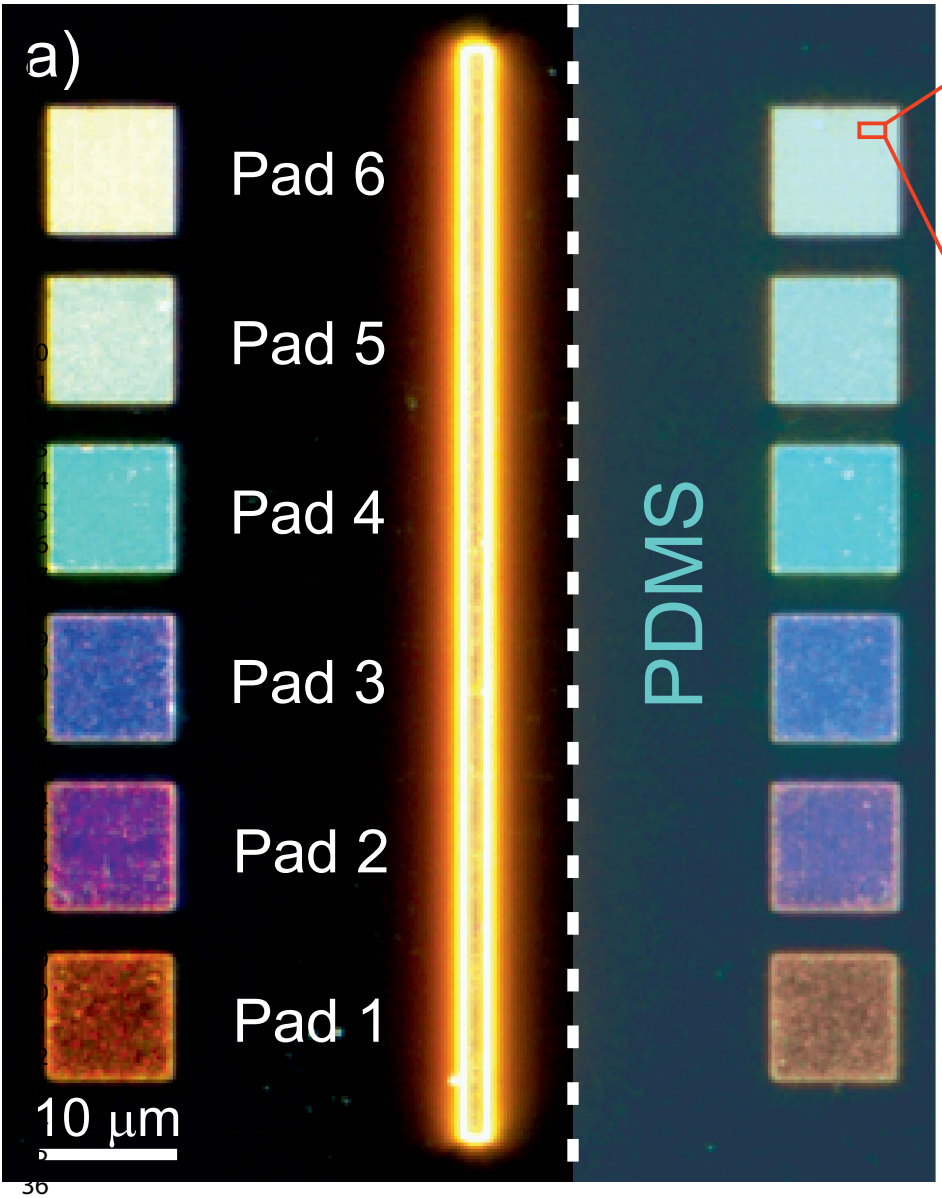
a)
Pad 6
Pad 5
Pad 4
Pad 3
Pad 2
Pad 1
PDMS
10 µm

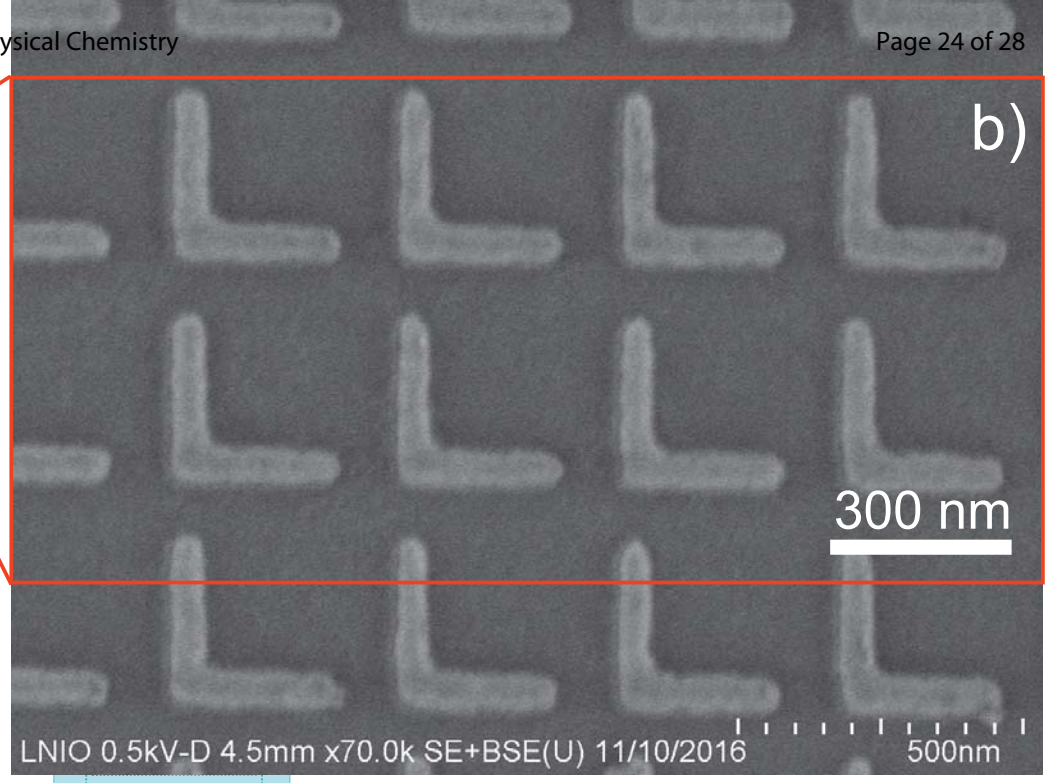
b)
300 nm
LNIO 0.5kV-D 4.5mm x70.0k SE+BSE(U) 11/10/2016
500nm

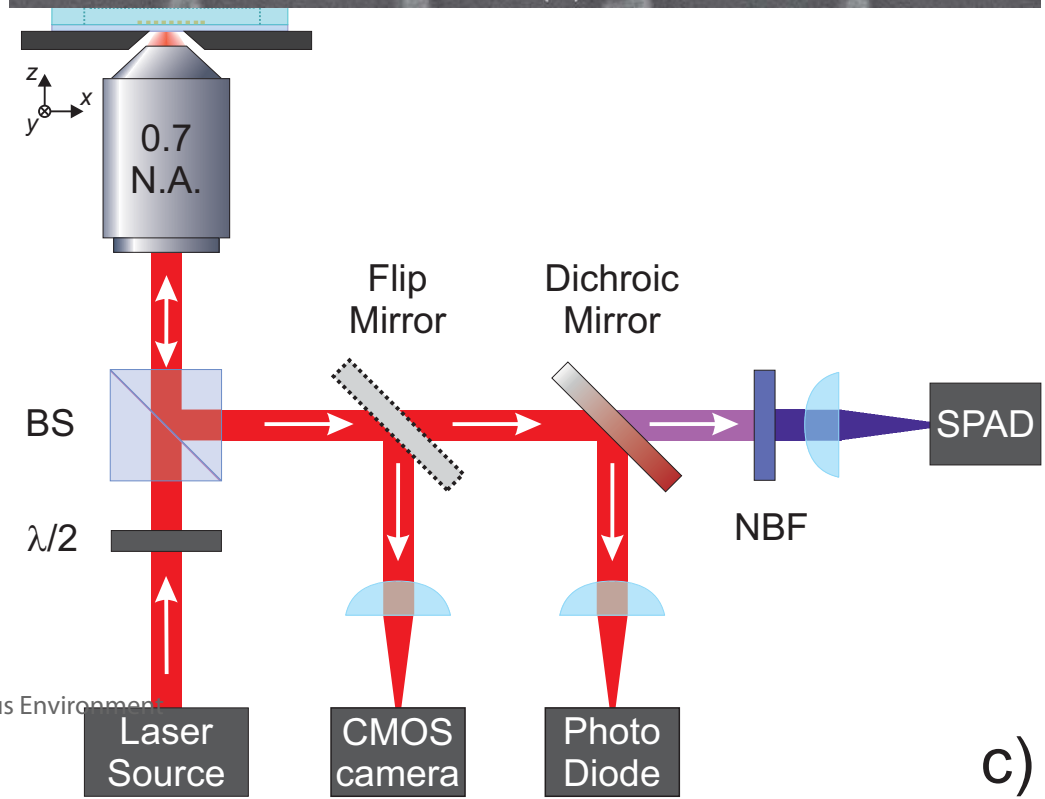
z
x
y
0.7
N.A.
Flip
Mirror
Dichroic
Mirror
BS
SPAD
NBF
λ/2
Laser
Source
CMOS
camera
Photo
Diode
c)

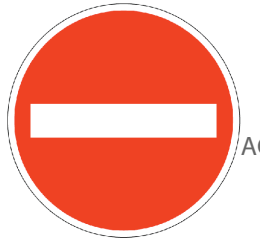

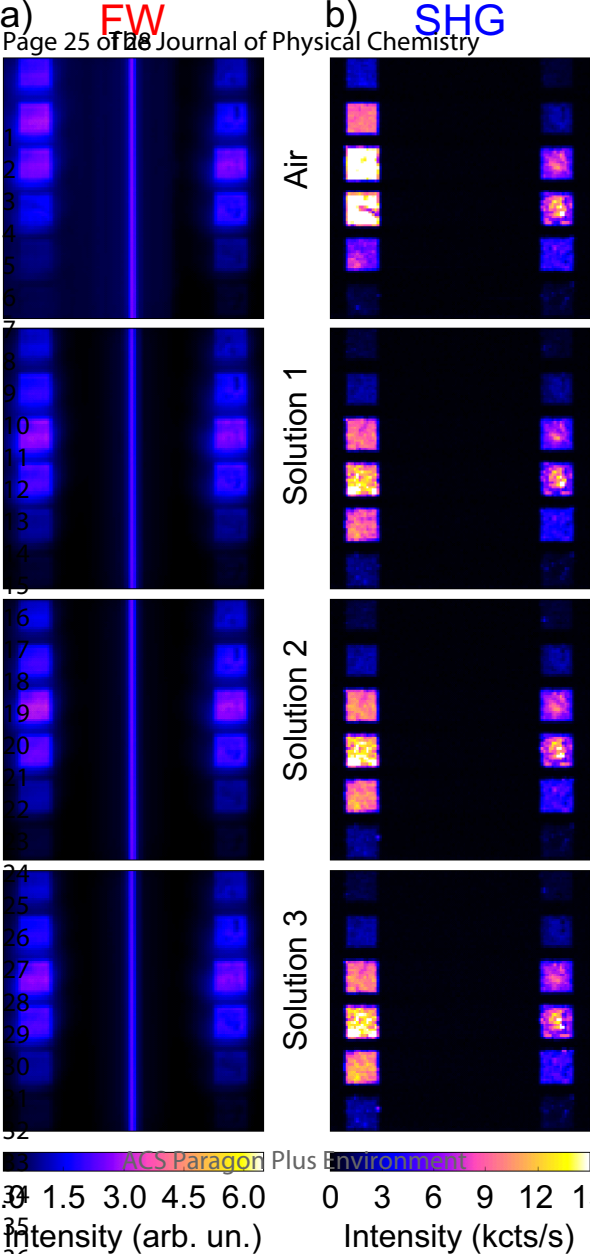

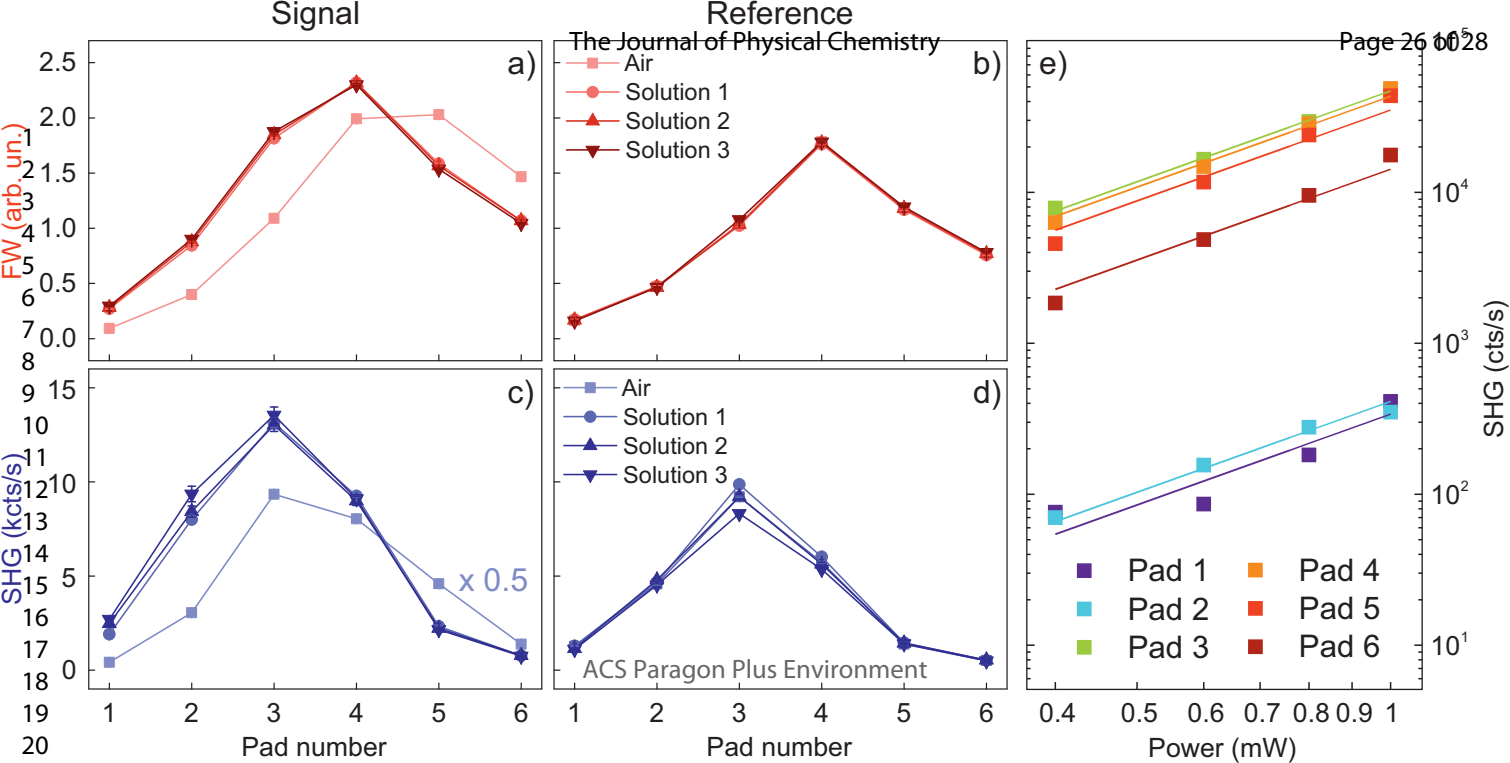
Signal
Reference
a)
b)
c)
d)
e)
FW (arb. un.)
SHG (kcts/s)
SHG (cts/s)
Air
Solution 1
Solution 2
Solution 3
x 0.5
Pad 1
Pad 2
Pad 3
Pad 4
Pad 5
Pad 6
Pad number
Pad number
Power (mW)
ACS Paragon Plus Environment